metals

MDPI

Article

Laser Powder Bed Fusion Additive Manufacturing of Fe_3Al-1.5Ta Iron Aluminide with Strengthening Laves Phase

Aliakbar Emdadi [1,*], Sebastian Bolz [2], Johannes Buhl [2], Sabine Weiß [1] and Markus Bambach [3]

[1] Chair of Physical Metallurgy and Materials Technology, Brandenburg University of Technology Cottbus-Senftenberg, D-03044 Cottbus, Germany; weiss@b-tu.de
[2] Chair of Hybrid Manufacturing, Brandenburg University of Technology Cottbus-Senftenberg, D-03044 Cottbus, Germany; bolzseba@b-tu.de (S.B.); johannes.buhl@b-tu.de (J.B.)
[3] Advanced Manufacturing Laboratory, ETH Zürich, Technoparkstr 1, 8005 Zürich, Switzerland; mbambach@ethz.ch
* Correspondence: emdadi@b-tu.de; Tel.: +49-(0)-355-69-2970

Abstract: Advanced aluminides strengthened with incoherent Laves phase precipitates are promising lightweight and creep-resistant alternatives for high-alloy steels and superalloys for high-temperature critical components up to 750 °C service temperature. A significant issue with manufacturing these aluminides with conventional casting is the strong coarsening tendency of the Laves phase precipitates at elevated temperatures, leading to a significant strength reduction. In this context, the short lifetime of the melt pool in additive manufacturing and its fast solidification and cooling rates promise to consolidate these aluminides with homogeneously distributed fine Laves phase particles without coarsening. The main scientific objective of this work is to exploit the unique characteristics of the laser powder bed fusion (L-PBF) additive manufacturing (AM) process to print dense and crack-free bulk Fe_3Al-1.5Ta samples containing uniformly distributed $(Fe, Al)_2Ta$ Laves phase precipitates. The Fe-25Al-2Ta (at.%) alloy was selected for this work since its creep resistance at 650 °C surpasses the one of the P92 martensitic–ferritic steel (one of the most creep-resistant alloys developed for steam turbine applications). Fundamentals on process–microstructure relationships governing the L-PBF-fabricated builds are provided by a detailed microstructural characterization using X-ray diffractometer (XRD) and ultra-high-resolution scanning electron microscopy (SEM) equipped with energy-dispersive X-ray spectroscopy (EDX) and high-resolution electron backscatter diffraction (EBSD) detectors. Orientation imaging microscopy (OIM) and grain reference orientation deviation (GROD) maps were applied to measure texture and visualize substructures within the grains. The mechanism of voids formation, morphology, and volume fraction as a function of the input energy density was identified. The melting and solidification dynamics led to microstructures with large columnar grains, porosity, and periodic cracks during the printing process. Processing samples at the building temperatures below the brittle-to-ductile transition temperature, BDTT (750 °C), often caused severe macrocracking and delamination. Crack-free samples with densities higher than 99%, some approaching 99.5%, were fabricated from pre-alloyed gas-atomized powders with a combination of high laser power (250–300 W), slow-to-medium scanning speed (500–1000 mm/s), and 800 °C build plate preheating using a 67° rotation scanning strategy. The morphology of the pores in the volume of the samples indicated a relatively sharp transition from spherical geometry for scanning speeds up to 1000 mm/s to crack-like pores for higher values. The ultra-fast cooling during the L-PBF process suppressed $D0_3$ Fe_3Al-ordering. The Fe_3Al-1.5Ta builds were characterized by B2 FeAl-type order clusters dispersed within a disordered A2 α-(Fe, Al) matrix. Additionally, the $(Fe, Al)_2Ta$ Laves phase ($C14–P6_3/mmc$) was predominantly formed at the matrix phase grain boundaries and frequently dispersed within the grains. The quantitative EDX analysis of the matrix gave 77.6–77.9 at.% Fe, 21.4–21.7 at.% Al, and 0.6–0.8 at.% Ta, while the composition of the Laves phase was 66.3–67.8 at.% Fe, 8.7–9.8 at.% Al, and 22.4–24.9 at.% Ta, indicating that the Laves phase is considerably enriched in Ta with respect to the matrix. The L-PBF-fabricated alloys were characterized by coarse, columnar grains which grow epitaxially from the substrate, were several m in width, and extended across several layers along the building direction. The grains exhibited a relatively strong

Citation: Emdadi, A.; Bolz, S.; Buhl, J.; Weiß, S.; Bambach, M. Laser Powder Bed Fusion Additive Manufacturing of Fe_3Al-1.5Ta Iron Aluminide with Strengthening Laves Phase. *Metals* **2022**, *12*, 997. https://doi.org/10.3390/met12060997

Academic Editor: Amir Mostafaei

Received: 27 April 2022
Accepted: 8 June 2022
Published: 10 June 2022

microtexture close to <0 0 1> with respect to the building direction. The L-PBF builds showed a bulk hardness value comparable to the as-cast and spark plasma-sintered counterparts. A negligible variation of the hardness across the build height was observed. Within the framework of this study, we demonstrated that the porosity and cracking issues could be resolved mainly by controlling the process parameters and preheating the build platform above the BDTT. Nevertheless, alloy modifications and/or post-manufacturing processing are required for microstructure refinement.

Keywords: laser powder bed fusion; iron aluminide; Laves phase; microstructure; porosity; electron backscatter diffraction

1. Introduction

Intermetallic compounds of iron aluminides may address a key challenge of the aviation and power generation industries to develop more creep-resistant and lightweight alloys as a replacement for heavy and partly expensive conventional superalloys. It increases the operating temperature and reduces the weight of rotating parts, enhancing the thermal efficiency of the aircraft engines and steam turbines. Ultra-supercritical steam turbines are aimed to operate at an increased temperature of 750 °C and steam pressure up to 35 MPa [1]. A critical issue is the limited creep properties of current ferritic steels at the targeted elevated temperatures. Polycrystalline Ni- and Co-based superalloys are possible solutions; however, they are much heavier than steels. Advanced iron aluminides are promising replacements, since they feature lower densities than commercial structural materials and high strength and creep resistance up to at least 800 °C [1,2]. This increase in the thermal efficiency of steam turbines could lead to a significant cost saving annually and a drastic decrease in fuel consumption and environmental issues by lowering CO_2 emissions from fossil-energy power plants. In addition to the potential use for higher-performance aero-engine rotational applications, iron aluminides were also found to meet the demand for sustainability in the marine industry. An Fe-Al-Mo-Ti-B alloy strengthened with Mo_2FeB_2-type borides was recently proved to be an economical alternative to the currently used Ni-based alloys in the combustion chamber of large-bore 2-Stroke marine engines [3].

Fe–Al-based alloys, i.e., alloys which contain either disordered A2 α-(Fe, Al), B2-ordered FeAl, or $D0_3$-ordered Fe_3Al as majority phases, have long been considered excellent candidates to replace heat-resistant steels or possibly even superalloys in high-temperature applications up to 800 °C, primarily because of their excellent oxidation and corrosion resistance even in aggressive environments [1,2,4,5]. They have a lower density and are less expensive than steels and superalloys; however, they exhibit low strength at temperatures above 800 °C [6,7]. Concepts derived from the phase diagram were studies for the strengthening of Fe–Al-based alloys, including solid-solution hardening, strengthening by precipitates, and ordering [8]. Specifically, strengthening by intermetallic Laves phases is one of the concepts leading to improving the high-temperature mechanical properties of iron aluminides [1,5,9,10]. The addition of alloying elements (A), including Nb [11,12], Ta [13,14], Ti [15], or Zr [16], leads to the formation of a Laves phase in a thermodynamic equilibrium with the iron aluminide matrix. The resulting C14 $A(Fe, Al)_2$ Laves phases precipitate as fine incoherent particles from the supersaturated aluminide matrix phase or form a eutectic mixture depending on the alloying quantity [17]. A significant issue with applying these aluminides at elevated temperatures is the strong coarsening tendency of the Laves phase particles [17]. Microalloying with trace quantities of B and C appeared beneficial to control the precipitation and growth of Laves phase particles through the formation of borides [18] or carbides [19].

In the alloying series of Fe-25Al-xTa (x = 0.5–6 at.%, all compositions are given in atomic percent throughout the text unless otherwise stated), the Fe-25Al-2Ta alloy was identified to be more qualified for structural applications at and above 600 °C than its binary

counterpart and other alloys of the series due to a superior creep resistance [1,10,13,20,21]. Surprisingly, the creep resistance of Fe-25Al-2Ta alloy at 650 °C surpasses the one of the P92 (X10CrWMoVNb9-2) martensitic–ferritic steel, which is one of the most creep-resistant alloys developed for steam turbine applications [20]. Oxidation experiments of Fe_3Al containing 2 at.% Ta showed an excellent oxidation resistance up to 800 °C [22].

State-of-the-art metal additive manufacturing (AM) allows the fabrication of near-net-shape complex geometries, which enables the realization of more efficient and lightweight designs, more sustainable part manufacturing, fast prototyping, and reduced machining costs [23–25]. Metal-based AM is a potentially disruptive technology across multiple industries, including aerospace, biomedical, and automotive. Building up metal components layer by layer increases design freedom and manufacturing flexibility, enabling complex geometries, increased product customization, and shorter time to market, while eliminating traditional economy-of-scale constraints [26].

AM has been introduced as a powerful tool for the aerospace industry. A case study reported that AM could reduce jet engine air manifold production costs by optimizing the design and reducing the machining costs [27,28]. AM also offers new opportunities for creating novel materials with unique properties, such as composite materials, multiple materials, functionally gradient materials, and even metamaterials [29]. AM technologies also have great potential to address global energy challenges and are applied in nuclear energy, batteries, fuel cells, and oil and gas [30]. The effect of AM on global energy demand was assessed using a bottom-up approach, and it was revealed that AM will contribute to a 5–27% reduction in global energy use in 2050, and potential energy savings in aerospace and construction are 5–25% and 4–21% by 2050 [31].

In the laser powder bed fusion (L-PBF) process, also known as selective laser melting (SLM), a focused laser beam selectively melts a layer of metal powder. After consolidation, the second layer of metal powder is applied and metallurgically bonded to the previous layer. This cycle's repetition enables the tool-free manufacturing of complex geometries in a relatively fast time with a minimum of waste [32].

The AM process can be regarded as a multipass weld suffering from the weld defects such as hot tearing and high residual stresses. Therefore, materials that are particularly susceptible to weld-cracking, such as non-weldable nickel superalloys and intermetallics, cannot easily be manufactured via AM without significant hot cracking [33,34]. Several alloy modification, process control, and post-processing approaches have been utilized to mitigate hot cracking susceptibility for many alloys. For example, high-strength 7075- and 6061-series aluminum alloys could be processed successfully by SLM through alloy modification by 1 vol% hydrogen-stabilized Zr nucleants, producing crack-free materials with strengths double that of the most common additively manufactured aluminum alloy [26].

The mechanical properties of the additively manufactured parts are sensitive to various parameters, such as those of the AM method and the post-process heat treatment [35]. In general, AM-induced defects such as porosity and high thermal residual stresses often suppress the mechanical integrity of AM parts. The employment of optimized AM process parameters and the application of post-heat-treatment processes are beneficial for decreasing the AM-induced defects and residual stresses [36]. For example, it has been shown that the employment of optimized parameters for the AM process and the subsequent heat treatment process in combination with surface machining enhance the fatigue strength of AM Inconel 718 to even higher than that of the wrought alloy [36]. Alloy modification is another strategy to improve the mechanical properties of the as-built materials. For example, the creep rupture life and ductility of an IN718 superalloy produced by SLM were improved by the addition of yttrium (Y) through the formation of Y oxide (yttria) instead of Al-rich oxide and the suppression of δ-phase precipitate growth [37].

In another study, a methodology was proposed to control the fatigue life of 17-4Ph stainless steel by selecting the most relevant manufacturing parameters. The results showed that the fatigue limit of the specimens manufactured by SLM has reached near 90% of the value found in samples machined from a bar [38]. Sara Giganto et al. proposed

design recommendations for the precision SLM manufacturing of 17-4Ph parts. Regarding geometrical accuracy, it was recommended to avoid surfaces with 45° negative slopes or higher [39]. The benefit of producing parts from advanced iron aluminides by AM could be two-fold. Due to the high cooling rates, fine-grained microstructures could be achieved whereby the room temperature ductility of Fe_3Al-based alloys can be improved. Besides, the near-net-shape production of parts by AM will, in turn, reduce expensive machining costs of the difficult-to-machine Fe_3Al-based alloys. Several attempts at fabricating iron aluminides by additive manufacturing have been reported. C. Shen et al. [40] produced Fe_3Al alloy of consistent composition and full density using the wire arc additive manufacturing (WAAM) process, incorporating the in situ alloying of the elemental Fe and Al components. They also presented a method to use neutron diffraction to measure residual stresses in Fe_3Al components fabricated by WAAM with different post-manufacturing treatments [41]. A. Michalková et al. [42] investigated the laser AM of iron aluminides strengthened by various strategies of ordering (in Fe-30Al-10Ti), the precipitation of borides (in Fe-30Al-5Ti-0.7B), or a coherent $L2_1$ Heusler phase (in Fe-22Al-5Ti). They discovered that all three alloying strategies developed from as-cast alloys could be achieved through both selective laser melting (SLM) and laser metal deposition (LMD) processes, resulting in nearly defect-free and dense (>99.5%) samples. Th powder-based AM of Fe_3Al-based alloys was explored to produce Fe-28Al [43], Fe-30Al-0.35Zr-0.1B [44], and Fe-(25–40)Al-(10–20)Ti [45] alloys by laser-engineered net shaping (LENS). G. Rolink et al. [46] applied L-PBF and LMD techniques to produce samples from pre-alloyed gas-atomized Fe-28Al powder. Dense (>99.5%) samples were made using varied processing parameters and by preheating the substrate to 200–600 °C to prevent cracking during cooling. Despite the high cooling rates, the L-PBF-built samples showed coarse grains elongated along the building direction (BD). Such an anisotropic microstructure brings anisotropic mechanical properties, depending on whether the specimens were loaded along the BD or perpendicular to it.

A significant issue with manufacturing Laves precipitation-strengthened iron aluminides by conventional casting is the strong coarsening tendency of the Laves phase precipitates at elevated temperatures [17,47]. In this context, AM promises to consolidate these aluminides with homogeneously distributed fine precipitates due to its short lifetime of the melt pool and fast solidification and cooling rates. In the present work, we investigated the L-PBF of Fe_3Al-1.5Ta alloys with strengthening Laves phase precipitates for the first time to the best of the authors' knowledge. We selected this alloy composition as it showed a supervisor creep resistance at 650 °C to the one of the P92 martensitic–ferritic steel and excellent oxidation resistance up to 800 °C. The main objective of this work is to demonstrate the feasibility of printing dense and crack-free bulk Fe_3AlTa samples containing uniformly distributed $(Fe, Al)_2Ta$ Laves phase precipitates by the L-PBF process. Fundamentals on process–microstructure-property relationships governing the L-PBF alloy are provided by a detailed microstructural characterization using SEM/EDX, EBSD, OIM, XRD, and bulk Vickers hardness. The hardness variation across the build height is studied compared to those of the cast and SPS materials to evaluate the applicability of L-PBF as a valid alternative to standard processing routes. Such knowledge is vital, but the literature is lacking, considering the current interest and activity to employ advanced aluminides in aviation engines.

2. Materials and Methods

An alloy powder material with a nominal composition of Fe-25Al-1.5Ta was produced by gas atomization by NANOVAL GmbH & Co. KG, Berlin, Germany. The particle size distribution of the powder material is shown in Figure 1. The powder batch with a fraction size of +10/−45 µm and an average particle size of d_{50} = 22.6 µm was selected for further processing by L-PBF.

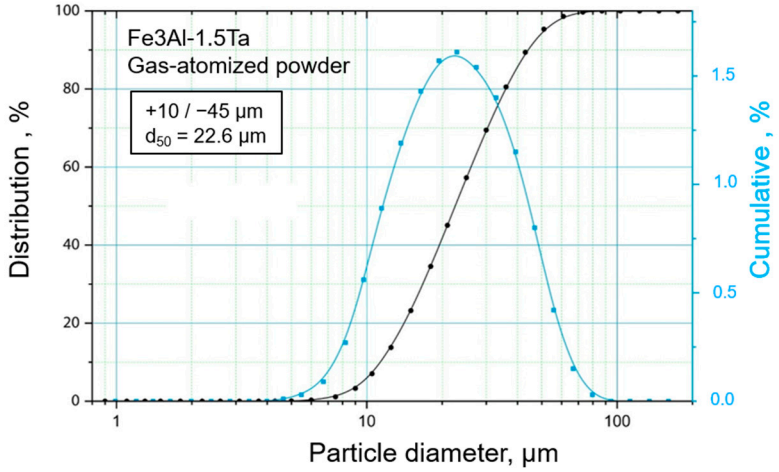

Figure 1. Distribution of Fe-25Al-1.5Ta alloy powder particle size produced by gas atomization.

Figure 2a,b show the BSE-SEM micrograph of the initial loose particles. The Fe-25Al-1.5Ta alloy powder particles are characterized by spherical morphology, with relatively smooth surfaces exhibiting a typical dendritic microstructure. The BSE-SEM and EBSD micrographs of the embedded particles in Figure 2c,d exhibit that the powder particles are composed of matrix grains decorated by a white contrast phase, located mainly at the boundaries of the matrix grains. The grains are almost equiaxed in shape, with an average size of 4.5 µm, and showing no preferred crystallographic orientation.

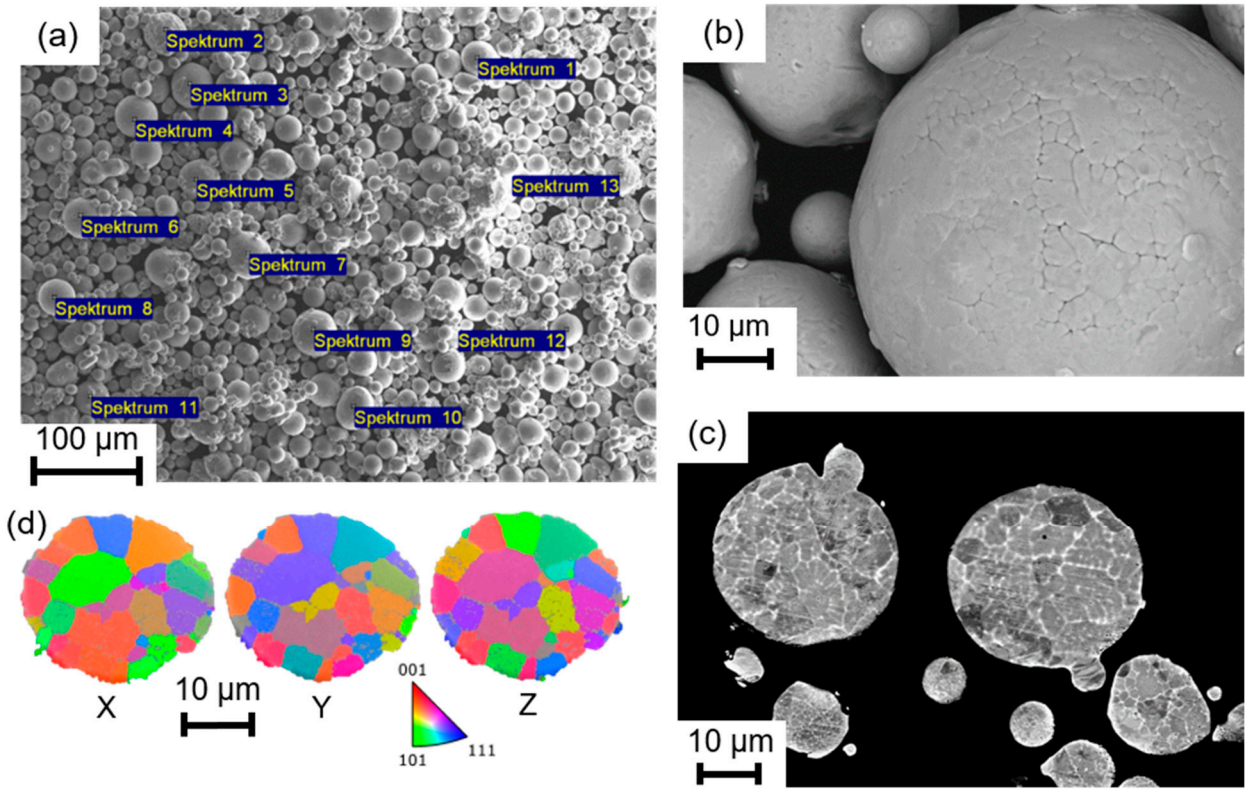

Figure 2. BSE-SEM micrographs of the loose (**a**,**b**) and embedded (**c**) particles and EBSD inverse pole figure (IPF) maps (**d**) of the Fe-25Al-1.5Ta alloy powder particles used to fabricate the L-PBF samples.

The results of the EDX analysis performed on several powder particles numbered in Figure 2a indicate that the average composition of the powder marginally deviates from the nominal composition (Table 1).

Table 1. The average concentration of the constituting elements measured by EDX on several powder particles marked in Figure 2a.

Elements Concentration, at.%		
Al	**Fe**	**Ta**
23.54 ± 3.30	74.77 ± 3.52	1.67 ± 0.42

The L-PBF experiments were performed with a 400 W AconityMIDI (Herzogenrath, Germany) laser source equipped with a 400 W single-mode laser of 80 µm-spot diameter and 1070 nm wavelength. The process was conducted in a chamber under the argon atmosphere. The oxygen content amounted to less than 200 ppm during processing. The typical parameters of L-PBF are listed in Table 2. Layer thickness and hatching distance were set to 50 µm and 90 µm, respectively. The process parameters such as laser power (P) and scanning speed (v_s) were varied between 500 and 1500 mm/s in steps of 250 mm/s and from 200 to 300 W in steps of 50 W. A stainless-steel plate with a thickness of 10 mm was used as substrate material. Intermetallic aluminides are prone to cracking; therefore, a high-temperature preheating during the AM process is required to reduce thermal gradients and suppress crack formation [48]. The processing of crack-free iron aluminides required a high-building temperature of 400 to 600 °C for LMD and 600 to 800 °C for SLM samples [42]. The brittle-to-ductile transition temperature (BDTT) of Fe_3Al-2Ta-cast alloy occurs at 750 °C [49]. Therefore, the formation of the cracks during cooling is most likely by processing the alloy below this temperature. We processed a few samples without preheating and a few at the building temperatures of 300–500 °C, and we noticed severe macrocracking and delamination of the samples from the build plate after printing a few layers. Therefore, a higher temperature of 800 °C was selected for preheating the steel plate to reduce temperature gradients and thermal stresses. Specimens of 8 × 8 × 8 mm^3 were built with a strategy illustrated in reference [50]. Parallel stripes with a width of 5 mm were used with the scan vectors on successive layers rotating at an angle of 67°.

Table 2. Typical process parameters adapted for L-PBF.

Beam Diameter	Scan Speed	Laser Power	Layer Thickness	Hatching Distance	Substrate Preheating
80 µm	500–1500 mm/s (increment 250)	200–300 W (increment 50)	50 µm	90 µm	800 °C

The phase identification was performed by a Bruker D8 ADVANCE X-ray diffractometer (Bruker, Billerica, MA, USA) using Cu-$K_{\alpha 1}$ radiation (λ = 0.15406 nm) within the 2θ range of 20–120° with a step size of 0.1°, and high-resolution scans in the range 25–35° were carried out with a smaller step size of 0.05°. Crystallographic data [51,52] for the present phases in Fe-25Al-1.5Ta are listed in Table 3.

Table 3. Crystal structure data for the present phases in Fe-25Al–2Ta alloy.

Phase	Pearson Symbol	Space Group No.	Structure Designation	Prototype
α-Fe	*cI2*	$Im\bar{3}m$	A2	W
FeAl	*cP2*	$Pm\bar{3}m$	B2	CsCl
Fe_3Al	*cF16*	$Fm\bar{3}m$	$D0_3$	BiF_3
$TaFe_2Al$, Heusler phase	*cF16*	$Fm\bar{3}m$	$L2_1$	$MnCu_2Al$
$TaFe_2$, Laves phase	*hP12*	$P6_3/mmc$	C14	$MgZn_2$

The macrostructures of the L-PBF-fabricated specimens sectioned parallel to the BD were investigated by light optical microscopy (LOM; VHX Digital Microscope, KEYENCE America, Itasca, IL, USA). Microstructures of the samples were characterized by field-free ultra-high-resolution (0.9 nm at 15 keV, 1.3 nm at 1 keV) scanning electron microscopy (SEM) on a TESCAN AMBER (Brno, Czech Republic) equipped with energy-dispersive

X-ray spectroscopy (EDX; Oxford Instruments, Abingdon, UK) and high-resolution electron backscatter diffraction (EBSD; Oxford Instruments Aztec system, Abingdon, UK) detectors. The SEM was operated with a beam current of 100 nA and an accelerating voltage of 15 kV. High-angular resolution EBSD data were recorded at a 1.18 µm-step size and analyzed using the AZtecCrystal software (AZtec 4.3, Oxford Instruments Aztec system, Abingdon, UK). Inverse pole figure (IPF) maps parallel to the BD were recorded to study the crystallographic orientations.

The low- and high-angle grain boundaries (LAGBs/HAGBs) were identified with a misorientation of 2–10° and more than 10°, respectively. The individual grains were outlined with a threshold angle of 10°, and the grain size was given as equivalent circle diameter (ECD).

EBSD orientation imaging microscopy (OIM) maps were employed to estimate texture and visualize the substructures within grains. In the current study, we applied a grain reference orientation deviation (GROD) axis and GROD-angle maps to visualize local intercrystalline distortions within the grains. The grain reference orientation deviation (GROD)-axis map displays the orientation heterogeneities that evolve in the samples [53]. For each pixel within the grain, the misorientation of the point relative to a reference orientation for the grain to which the pixel belongs is calculated and displayed as a color according to the IPF color key. The GROD-angle map is particularly useful for highlighting angular deviations in grains with even the smallest orientation angle pixel by pixel. GROD-angle maps are generated by determining the average orientation for each grain based on the user-defined grain detection. The deviation from this mean orientation is then plotted for each pixel.

The bulk Vickers hardness testing was performed with a LM 800AT LECO Microhardness Tester (LECO Corporation, St. Joseph, MI, USA) applying 2 kg force for a dwell time of 13 s. Hardness measurements were carried out on different regions of the samples, and an average of five measurements was reported. For comparison, the hardness values of the as-cast and spark plasma-sintered materials with the same chemistry are also reported [47]. An ingot with a diameter of 30 mm was cast using an investment casting procedure by Access e.V. (Aachen, Germany) [47]. Spark plasma sintering was conducted at 1200 °C for a holding time of 5 s under a compaction force of 35 kN by an FCT System GmbH (Effelder-Rauenstein, Germany) using the same powder batch used for the L-PBF operations. For more details on the microstructure of the as-cast and SPS materials, the readers are referred to references [14,47].

3. Results and Discussion

3.1. Effect of L-PBF Processing Parameters on the Porosity Formation and Morphology

L-PBF process is prone to melt pool instability due to the full melting mechanism, which, along with poorly chosen process parameters, can result in microstructural defects and porosity [54]. Processing parameters significantly contribute to the final porosity, microstructure formation, and properties of the fabricated parts. Preliminary research has been carried out to fabricate the Fe_3Al sample with the lowest possible porosity, an absence of cracks, and a sound reproduction of the model's shape by the proper selection of LENS-process parameters [44].

For a given material, laser energy density, E, is the energy provided by the laser beam to a volumetric unit of powder material and is given by:

$$E = \frac{P}{v_s \times h \times t}$$

where P is the laser power (W), v_s is the laser scanning speed (mm/s), h is the hatching distance (mm), and t is the layer thickness (mm). When incident energy density (E) increases, a large amount of melt is supplied, increasing the final density. An accurate adjustment of the processing parameters is mandatory for the manufacturing of fully dense components.

The energy density in the L-PBF process resulting from the laser power, scan speed, and hatch distance significantly influences the crack formation and residual porosity. Figure 3 exhibits an iso-contour processing map of the L-PBF-fabricated samples, showing the variation of the residual porosity as a function of the laser power and scanning speed. Insets display the typical LOM macrographs of cross-sections of the samples built with different processing parameters. The macroscopic cracking caused some samples to delaminate from the substrate (not shown here). The disintegration of the specimens due to high thermal stress was occasionally observed during processing with low laser power. The cracks originating from notches at the lateral surface were not observed, while unmelted powder particles were found in some samples. Generally, at a constant P, the energy input decreases with increasing v_s; thus, the density of the samples decreases. On the contrary, when the v_s is kept constant, the energy input increases with increasing P; therefore, a higher density is achieved.

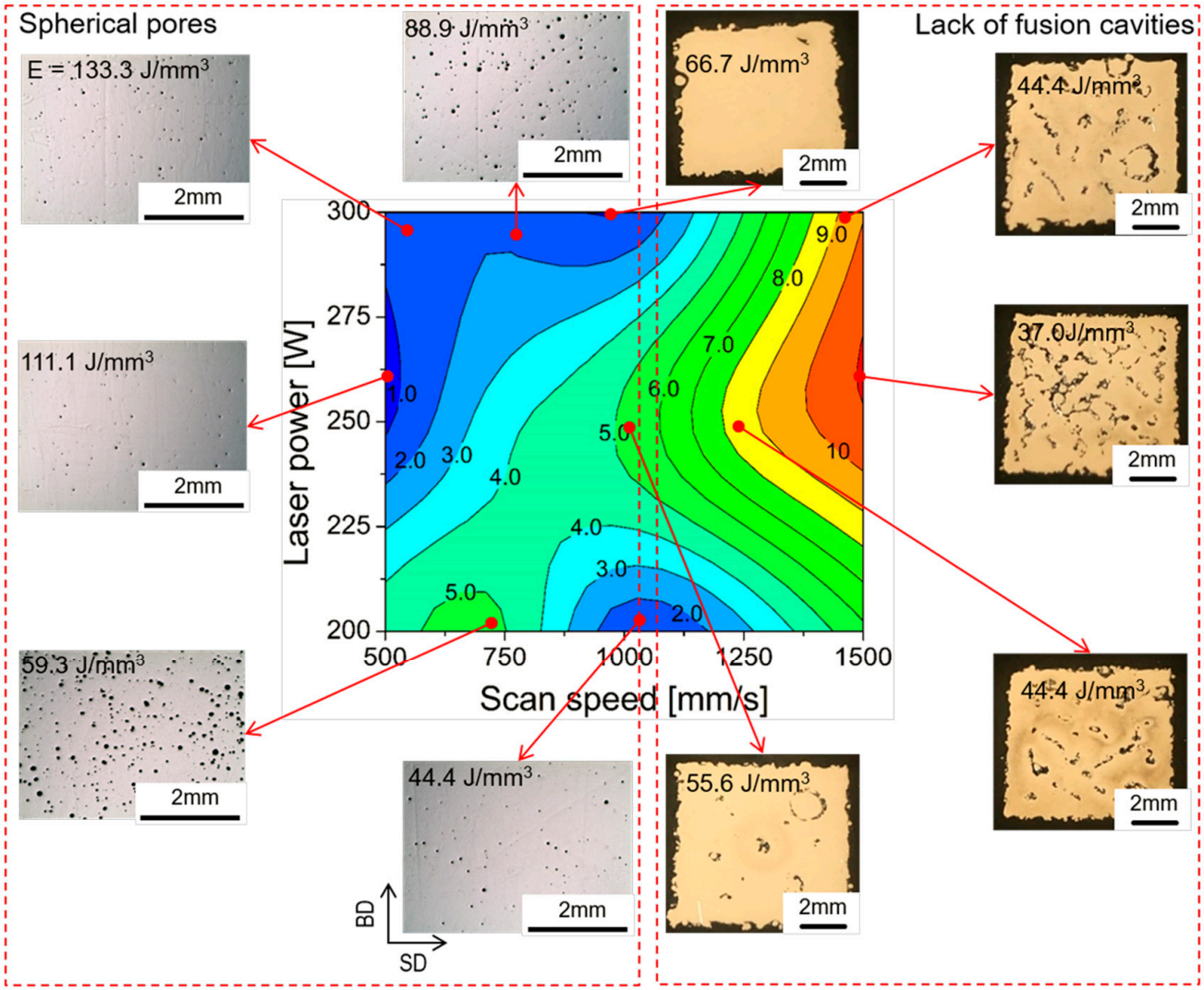

Figure 3. Iso-contour processing map of the L-PBF-fabricated samples showing the variation of the residual porosity as a function of the laser power and scanning speed. Insets display light optical macrographs of cross-sections of L-PBF-fabricated samples printed with different processing parameters. Regions delineated by red rectangles represent the domains dominated by spherical gas pores (**left**) and lack of fusion cavities (**right**). Contour values represent residual porosity in percent. BD and SD refer to the building and scanning directions. Input energy density associated with each sample is also given.

The morphology of the pores in the volume of L-PBF-fabricated samples generally changes from spherical for v_s up to around 1000 mm/s to crack-like pores for higher v_s values, as outlined by red rectangles in Figure 3. The sharp crack-like pores were associated with the lack of fusion (LOF) resulting from insufficient energy input or balling. In contrast, the spherical pores generally arise from entrapped gas and the keyhole effect [55,56]. In L-PBF-fabricated Ti-6Al-4V samples, gas pores up to 1 vol.% were found not to deteriorate the mechanical properties remarkably [57]. However, with an increased volume fraction of pores above 5%, tensile, fatigue, and hardness properties are significantly diminished [57]. The tight control of the cleanliness of metal powder feedstock and the atmosphere during metal powder production and the melting process can largely reduce the formation of gas pores.

LOF defects are irregularly shaped cavities that often contain trapped unmelted powder particles and are attributed to material discontinuity due to the insufficient penetration of the melt pool into the previous layer [58]. It was reported that LOF is critical to the fatigue properties and delamination of layers, among other defect types in additively manufactured Ti alloy parts [59]. A study of porosity formation in AlSi10Mg components fabricated by L-PBF using a combined experimental and finite element analysis approach showed that the large and irregular-shaped pores, especially those close to the surface, will dictate the component failure, most often by single dominating crack propagation [60].

The samples printed with process parameters 200 W–1000 mm/s, 250 W–1250 mm/s, and 300 W–1500 mm/s are subject to the same energy input of 44.4 J/mm^3, though they exhibit different pore morphology. The sample fabricated with 200 W–1000 mm/s contains spherical pores; however, the other two samples fabricated with a higher laser power (250–300 W) and scanning speed (1250–1500 mm/s) include crack-like pores. Considering the positive effect of laser power on the density of energy input, we can then conclude that the formation of crack-like pores is more likely at higher scanning speeds at a constant energy input density.

At energy densities of approximately 59.3−133.3 J/mm^3, samples without LOF defects and a low residual porosity of less than 5% could be produced. The samples with the lowest porosity values were obtained with high laser power (250–300 W) and slow-to-medium scanning speed (500–1000 mm/s). The specimens built at 300 W/1000 mm/s reach densities higher than 99%, with some approaching 99.5%. For the highest scanning speeds (1250−1500 mm/s) and lower laser power (250 W), the highest void fractions approaching 10−15% were observed.

3.2. Microstructure Characterization of the L-PBF-Fabricated Samples

According to the binary Fe–Al phase diagram [61], the $D0_3$-ordered Fe_3Al (α_1) is stable below 552 °C for alloys containing from 18 to 37 at.% Al; and the B2-ordered FeAl (α_2) occurs between 23 and 54 at.% Al depending on temperature. Both Fe_3Al ($D0_3$) and FeAl (B2) phases are bcc-derivative-ordered lattices, and they are separated from the disordered A2 solid solution by first-or second-order transitions [62]. A2 is a disordered body-centered (bcc) structure. B2 is an ordered structure with Al atoms occupying the body-centered sites ($Pm\bar{3}m$) and has the ideal stoichiometry of 50 at.% Fe-50 at.% Al. $D0_3$ ($Fm\bar{3}m$) is an ordered structure with the ideal stoichiometry of 75 at.% Fe-25 at.% Al, where the Fe atoms occupy the crystallographic 4a-(0,0,0) and 8c-(1/4,1/4,1/4) sites, while the Al atoms sit at the 4b-(1/2,1/2,1/2) sites with a doubling of the cubic cell parameter (i.e., the cell volume is increased by a factor of eight). The Fe atom in the 4*a* site has eight Fe-nearest neighbor atoms, while the Fe atom in the 8*c* site has four Fe atoms and four Al atoms as its nearest neighbors [63]. Further ternary ordering may lead to the formation of the $L2_1$ structure (Heusler phase), where the 4a and 8c sites are occupied by different transition metals or at least different mixtures of atoms. This structure type was reported in the ternary Al-Fe-Ti [64] and Al-Fe-Ta systems [65]. The primary X-ray diffraction lines of A2, B2, and $D0_3$ are identical, so identification is only possible based on a few relatively weak

superstructure reflections [66]. The phase identification of the superlattice structures is even more complicated when the phase presents as a minor component in a multi-phase sample.

Figure 4 exhibits the X-ray diffractograms of the L-PBF-built Fe_3Al-1.5Ta sample. The primary diffraction lines of different phases are also presented. The L-PBF builds are characterized by fundamental reflections of the disordered A2 α-(Fe, Al) phase and characteristic superstructure peaks of a (100) and (101) B2-type order structures occurring at around 21.29° and 30.79°, with no reflections from the $D0_3$-type order phase. The characteristic reflections of $(111)_{D03}$ and $(311)_{D03}$ should occur at around 26.68° and 52.41° using Cu-$K_{\alpha 1}$ incident radiation; however, they are not present in the XRD pattern of the L-PBF builds. Apart from the matrix reflections, peaks of the C14 Fe_2Ta Laves phase (also described as $(Fe, Al)_2Ta$ [13,20]) are found at around 2θ = 35.04 and 40.59°.

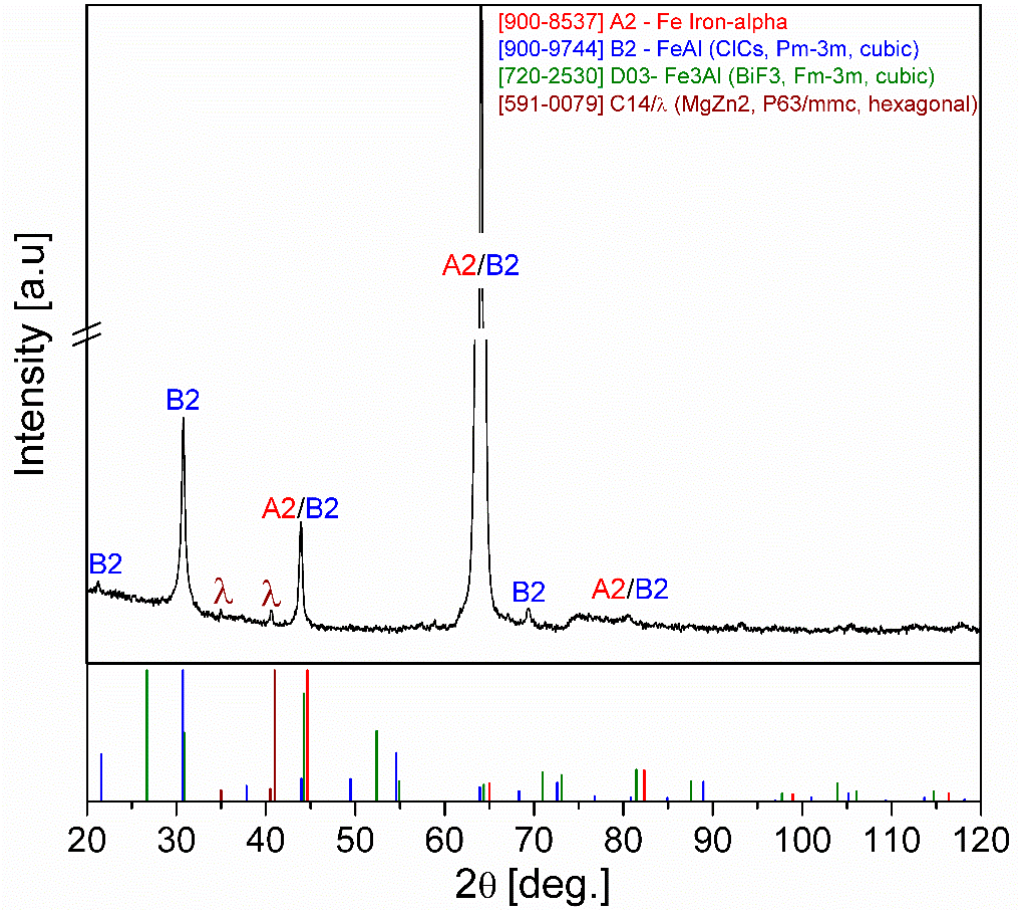

Figure 4. XRD diffraction patterns of the Fe_3Al-1.5Ta samples produced by L-PBF. A few characteristic reflections of A2 α-(Fe, Al), B2 Fe-Al, $D0_3$ Fe_3Al, and C14 $(Fe, Al)_2Ta$ phases are also presented.

The results of phase identification in the present study agree well with the literature. The presence of the metastable B2 and the suppression of the equilibrium $D0_3$ at room temperature was found typically for the Fe_3Al-based materials subjected to high-cooling-rate LENS fabrication [44,67]. Likewise, water quenching from 900 °C in the binary Fe-27Al alloy prevented $D0_3$ ordering at room temperature; however, it did not preserve the high-temperature A2 structure, and the sample had the B2 structure at room temperature, according to the neutron diffraction and XRD data [68,69]. In contrast, the phase identification results in the Fe-25Al-1.5Ta alloy produced with an investment casting procedure revealed the presence of the $D0_3$ order and the C14 Laves phase [70]. The results suggest that the ordering transition from B2 to a $D0_3$ phase may take place during casting but hardly occurs during ultra-high-cooling processing.

Due to the ultra-fast cooling during the L-PBF process, the disordered A2 phase is expected to be preserved to room temperature. Moreover, the L-PBF processing does not allow the transition of B2 to $D0_3$; therefore, the $D0_3$ ordering is suppressed, and B2 is preserved at room temperature. The L-PBF builds are thus characterized by a disordered A2 matrix containing the ordered B2 phase domains. This conclusion agrees well with A. Balagurov et al.'s work [71]. They employed a combination of high-resolution and in situ real-time neutron diffraction to investigate coherent atomic ordering in Fe_3Al-type alloys in a wide temperature range. They showed that the bulk polycrystalline $(Fe_{0.88}Cr_{0.12})_3Al$ alloy in the quenched state comprised a disordered A2 matrix embedded with dispersed clusters of the partially ordered B2 phase [71].

Noteworthy is that the ordering type was reported to have only a negligible effect on the tensile yield and ultimate tensile strength of the Fe_3Al–0.35Zr–0.1B alloy fabricated by the LENS technique [44]. Nonetheless, the samples of the $D0_3$ structure showed almost 15% higher elongation than the samples with the B2 ordering type at 650 °C.

Figure 5 presents typical BSE-SEM micrographs of the L-PBF-fabricated samples from different regions printed with process parameters P = 250 W and v_s = 1000 mm/s. The sample exhibits a characteristic columnar grain morphology of additively manufactured metallic materials [72]. The microstructure primarily consists of large columnar grains, elongated along the vertical BD through epitaxial solidification, as is typical for the FeAl and Fe_3Al parts fabricated by AM [40,46,73,74]. In addition, some isolated equiaxed grains are also visible. The first layers near the build plate consist of finer grains (bottom image). The middle section of the printed sample contains mainly large columnar grains with a few small grains among them. The growth of the columnar grains is stopped in the last layer of the sample due to the lack of further thermal cycling. Besides, a few small grains are observed near the top surface. Competitive growth of grains with different orientations occurs during the epitaxial grain growth [75]. The grains closely aligned with the maximum thermal gradient direction (the BD) dominate the epitaxial growth due to the grain selection. Columnar grains are unfavorable as they can impose solidification defects and mechanical property anisotropy. Nonetheless, the thermal conditions involved during additive manufacturing make columnar grains inevitable. The prevailing solidification conditions favoring epitaxial growth (from prior deposited layers) and a lack of nucleation events ahead of the solid/liquid (S/L) interface lead columnar grains to develop during AM [76].

As shown in a higher magnification image in Figure 5, the Fe-Al matrix grains are decorated by a phase with a white BSE contrast. According to earlier studies [14,70] and XRD results in Figure 4, this phase corresponds to the C14 Laves phase $(Fe, Al)_2Ta$ with hexagonal crystal symmetry. It was reported that the solubility of Ta in the binary Fe-Al phases is generally low and varies with Al content [49]. For example, the solubility of Ta in Fe-25Al alloys in equilibrium with Laves phase is about 0.7% at 1000 °C and 0.5% at 800 °C and less at lower temperatures [49]. Ta solubility increases in Fe-Al alloys with increasing Al content up to 40% Al [20,65]. An earlier study [20] indicated that the maximum Ta solubility in the Fe-Al matrix is about 5.1% at 1000 °C; thus, the addition of small amounts of Ta to Fe(Al) solid solution phases leads to the precipitation of the ternary Laves phase, resulting in extended two-phase fields. An experimental study and thermodynamic re-assessment of the binary Fe-Ta system revealed that the Laves phase forms through eutectic reactions L ↔ (δFe) + λ/C14 [52]. Thermo-Calc computations in Fe-25Al-1.5Ta alloy indicated that the C14 Laves phase formed through a eutectic reaction L ↔ α-(Fe, Al) + C14 at around 1150 °C and remained stable until lower temperatures around 570 °C during cooling [47]. The eutectic solidifies between the primary α-(Fe, Al) phase grains, therefore covering the boundaries of α-(Fe, Al) grains after solidification. Upon further cooling, the Laves phase transforms to the $L2_1$ $TaFe_2Al$ Heusler phase, a ternary equivalent of $D0_3$ Fe_3Al.

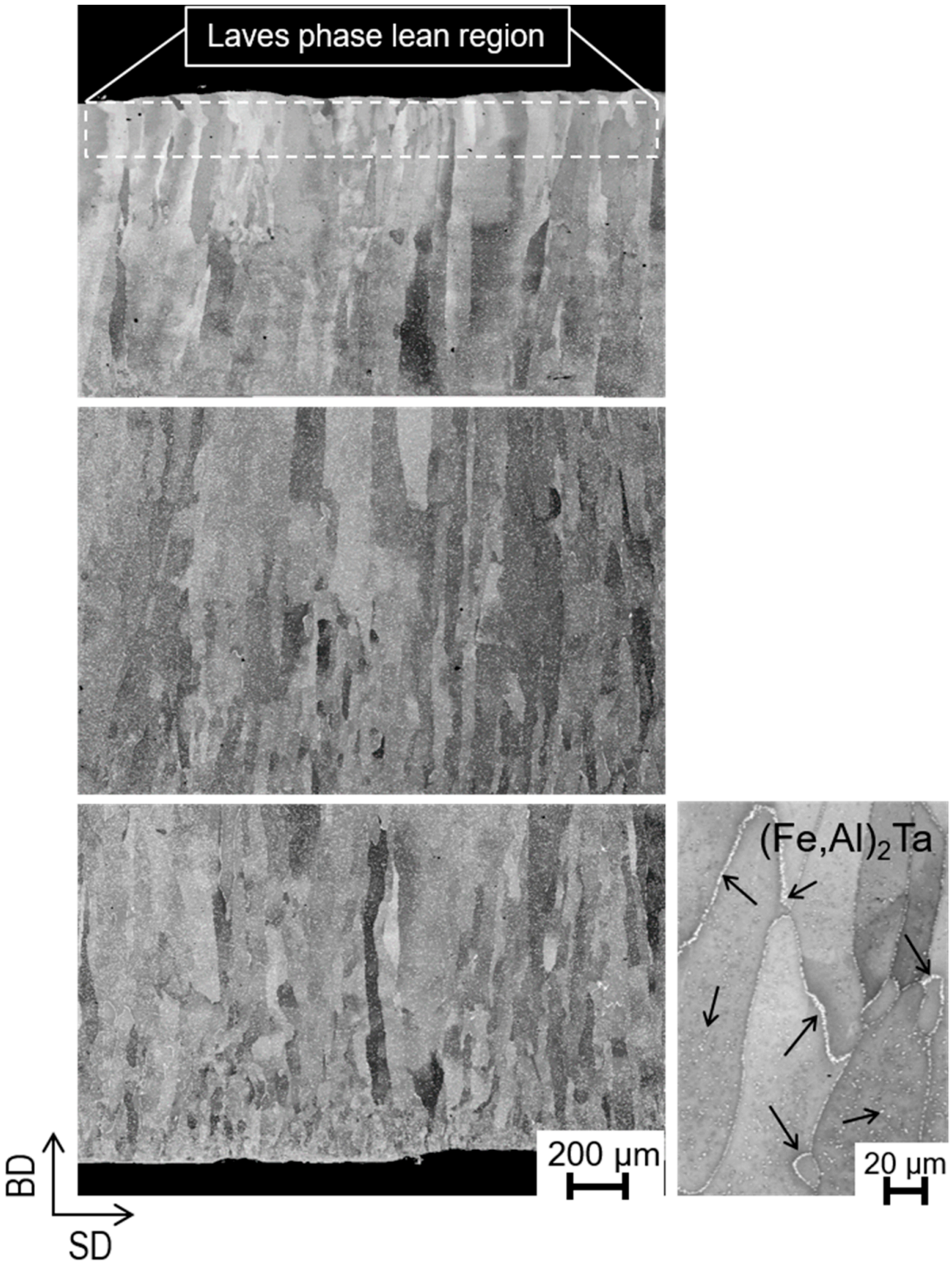

Figure 5. Typical BSE-SEM micrographs of the L-PBF-fabricated Fe_3Al-1.5Ta builds in the BD-SD cross-section at the interface with the substrate (bottom), middle, and top regions of the sample. The arrows in a high magnification image refer to several (Fe, Al)$_2$Ta Laves phase precipitates formed primarily at GBs and inside the matrix grains. The build was printed with process parameters: P = 250 W and v_s = 1000 mm/s. The BD and SD refer to the building and scanning directions. The region marked by a white rectangle at the very top represents a few layers that hardly contain Laves phase precipitates.

It was reported that the Laves phase primarily precipitated on the Fe-Al grain boundaries and was occasionally observed inside the matrix grains in the as-cast Fe-25Al-2Ta alloys [47,49]. In contrast to the as-cast alloy, the builds in the present study also contain a significant amount of Laves phase particles finely dispersed within the grains in addition to the precipitates formed at the Fe-Al grain boundaries. Likewise, Laves phase particles appear coarser in the L-PBF builds than in the as-cast material. We can thus surmise that the repetitive heating cycles experienced by the builds during the L-PBF process likely led to enhanced precipitation and particle coarsening. Further investigation is required to verify this hypothesis.

The substrate preheating reduces along with the building height, affecting the precipitation phenomenon. Ultra-fast cooling during L-PBF largely suppresses Ta segregation and the Laves phase formation and preserves the supersaturated FeAlTa solid solution at lower temperatures. Upon a further heating cycle, the Ta-enriched Laves phase precipitates mainly along the boundaries of the matrix grains and within the grains. At the very top layers of the builds, as marked by a white rectangle in Figure 5, the strengthening Laves phase concentration is much less than that in the bottom and middle regions due to the lack of sufficient heating cycles for Laves phase precipitation at the top layers. The very top layers (100 μm) of the builds hardly contain the Laves phase. A similar difference in the strengthening phase concentration (γ'') across the build height was reported in the direct laser-deposited alloy 718 to cause hardness variation with height [77,78]. The hardness variation across the building height in the present L-PBF-fabricated samples will be discussed later in Section 3.3.

During metal AM processes, the local thermal history induced by the complex energy input procedure impacts microstructure, defects, residual stresses, and material performance [79]. K. Karczewski [80] investigated the effect of the cooling rate on grain morphology and texture in Fe-28Al samples produced by the LENS process. They found that the deposited materials were mainly characterized by the large columnar grains spread over several layers along the BD within the range of cooling rates investigated (0.6×10^4 to 3.5×10^4 K/s). An increase in the cooling rate formed few equiaxed grains and slightly reduced the columnar grain size. Moreover, the <0 0 1> texture was dominant in the builds regardless of the variations in the cooling rate.

Table 4 presents the average concentration of the constituting elements of the Fe-Al-Ta matrix phase and the $(Fe, Al)_2Ta$ Lave phase precipitates measured by EDX. The quantitative analysis of the matrix area gives 77.6–77.9 at.% Fe, 21.4–21.7 at.% Al, and 0.6–0.8 at.% Ta, while the composition of the Laves phase is 66.3–67.8 at.% Fe, 8.7–9.8 at.% Al, and 22.4–24.9 at.% Ta. An EDX line scan analysis around a Laves phase precipitate at a grain boundary triple junction in Figure 6a,b indicates that the Laves phase is considerably enriched in Ta with respect to the matrix. The EDX elemental mapping in Figure 6c demonstrates that the distribution of the elements inside a Laves phase precipitate is relatively uniform.

Table 4. The average concentration of elements within the Fe-Al-Ta matrix and $(Fe, Al)_2Ta$ Laves phase determined by EDX.

Phase	The Concentration of Elements, at.%		
	Al	Fe	Ta
A2 α-(Fe, Al, Ta) matrix	21.5 ± 0.1	77.8 ± 0.1	0.7 ± 0.1
C14 $(Fe, Al)_2Ta$ Laves phase	9.1 ± 0.5	66.8 ± 0.7	24.2 ±1.2

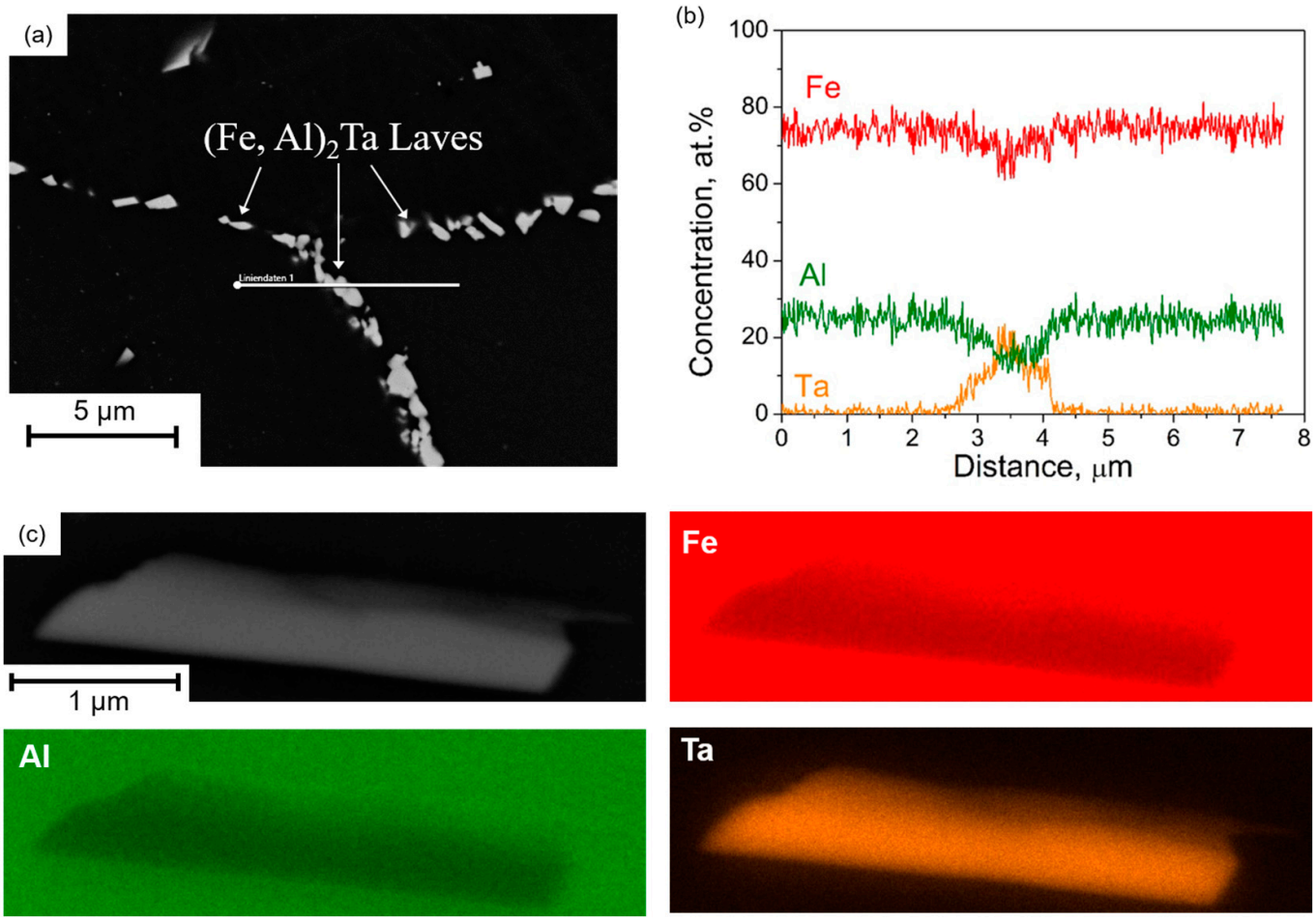

Figure 6. EDX line scan analysis around the (Fe, Al)$_2$Ta Laves phase precipitated at a grain boundary triple junction (**a**,**b**), and EDX elemental mapping inside a Laves phase precipitate (**c**) of the L-PBF Fe_3Al-1.5Ta builds printed with process parameters: P = 250 W and v_s = 1000 mm/s.

Figure 7 exhibits EBSD inverse pole figure (IPF) maps superimposed with GB misorientation maps from different regions of the L-PBF-fabricated Fe_3Al-1.5Ta sample along the BD. The as-built specimens exhibit a columnar grain morphology extended over several layers and oriented toward the BD. These elongated grains indicate an epitaxial solidification and growth mechanism, yet the epitaxial microstructure is often impeded at the solidification front by developing new grains with random crystallographic orientations. The first layers near the sample–substrate interface consist of finer grains (bottom image). However, a selection of grains occurs during further built-up, leading to coarsening and the formation of elongated grains of several hundred micrometers in length. In the lower region of the sample, some grains grew across seven layers (350 µm), while in the middle and upper areas, grains with a length of up to 1250 µm are found (25 layers). The grain size distribution is inhomogeneous throughout the sample, ranging from 4.4 to 360 µm for the bottom, from 5.8 to 615 µm for the middle, and from 4.8 to 629 µm for the top parts. In the lower, middle, and upper regions, the average grain size (equivalent circle diameter) is about 202 µm, 564 µm, and 448 µm, respectively. Large temperature gradients and fast cooling rates during L-PBF lead to the growth of elongated grains along the BD. The epitaxial growth of the large columnar grains along the build-up direction is in good agreement with the literature, where long grains of several hundred micrometers were documented for Ti–6Al–4V [81] and Fe-28Al [46] samples processed by L-PBF.

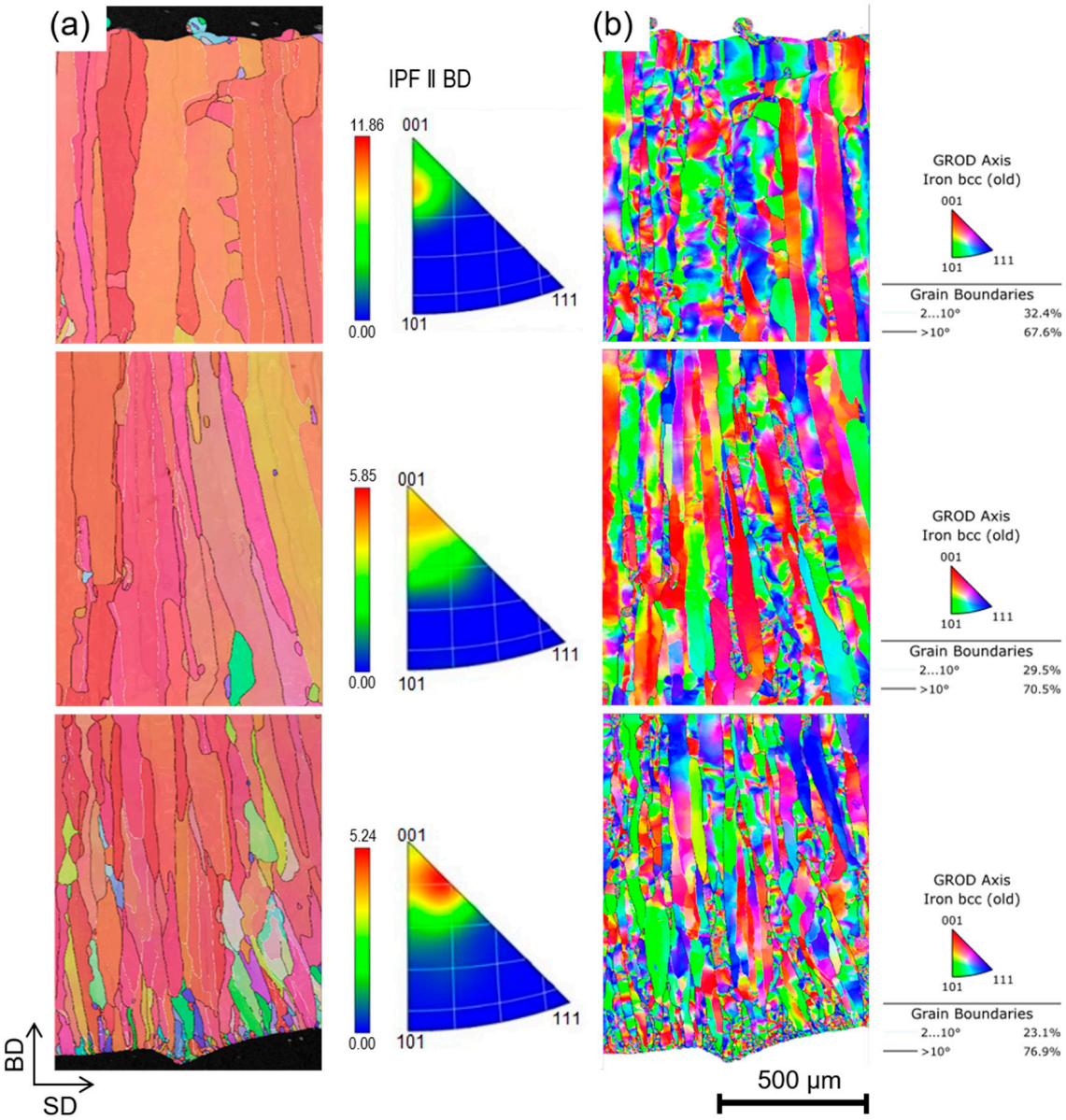

Figure 7. EBSD IPF (**a**) and GROD-axis (**b**) maps superimposed with GB misorientation maps from different regions of the L-PBF-fabricated Fe_3Al-1.5Ta builds along the BD. The BD and SD refer to the building and scanning directions. High- and low-angle grains are outlined with black and white boundaries. Grains were constructed assuming a 10° tolerance angle. The sample was printed with process parameters: P = 250 W and v_s = 1000 mm/s.

The successive melting and epitaxial solidification cycles lead to the formation of a textured columnar microstructure due to the competitive growth of the grains. The EBSD IPF maps reveal that the crystallographic orientation changes from random at the sample base to a preference close to <0 0 1> orientation (red color) in the upper regions with respect to the BD. A similar texture was reported for the binary Fe_3Al alloys processed by L-PBF [46]. Besides, most of the grains show a continuous variation of the color in the BD. The grain boundary misorientation maps indicate a significant amount of HAGBs, delineated by black lines, through the entire sample thickness along the BD.

Very high solidification and cooling rates and repeated abrupt heating and cooling cycles generate the build-up of anisotropic microstructures and residual stresses during metal powder bed fusion [82]. The magnitude of these stresses resulting from PBF processing is generally large, sometimes approaching the material's yield strength due to the high

and localized energy of the laser/electron beam heating. The build-up of residual stress is accommodated by the formation of dislocations that produce local crystallographic misorientation within grains; thus, it can be observed in orientation imaging microscopy (OIM) images [53]. Terner et al. [83] used average misorientation maps to visualize the residual stress levels of a superalloy 625 produced by L-PBF and subsequent heat treatments. They reported that EBSD could be effectively used to investigate the amount and distribution of strain energy levels caused by dislocations produced to accommodate the significant thermal stresses during L-PBF. Likewise, Nolze et al. [84] showed that EBSD is a reliable analytical method to visualize the comparatively big lattice rotations within additively manufactured materials.

In the current study, we applied grain reference orientation deviation (GROD)-axis and GROD-angle maps to visualize local lattice curvatures and substructures within the grains. Local intercrystalline distortions are correlated with residual stresses developed during L-PBF. The GROD axis calculates the misorientation axis for each pixel within a grain with respect to the average orientation of the grain and displays it as a color according to the IPF color key. The GROD axis helps to highlight the rotation axes to show the preferred crystallographic direction independent of the grain size. Figure 7b represents the GROD-axis maps superimposed with GB misorientation maps from different L-PBF-fabricated Fe_3Al-1.5Ta sample regions along the BD. Individual grains are composed of a few subregions with distinctive orientations correlated with the local lattice rotations arising from the high residual stress levels during L-PBF.

The GROD-angle map is particularly useful for highlighting angular deviations in grains with even the smallest orientation angle pixel by pixel. In Figure 8, the GROD-angle map taken from the middle part of the L-PBF-fabricated sample is displayed, reflecting considerable lattice rotations within the sample as high as about 14°. Likewise, a large orientation deviation is visible within individual grains, manifested as a change in color. The inset exhibits cumulative disorientation along the white arrow across an elongated coarse grain within a distance of 500 µm. Disorientations as high as 6° are observed across the grain, reflecting significant intercrystalline lattice rotations accumulated during L-PBF.

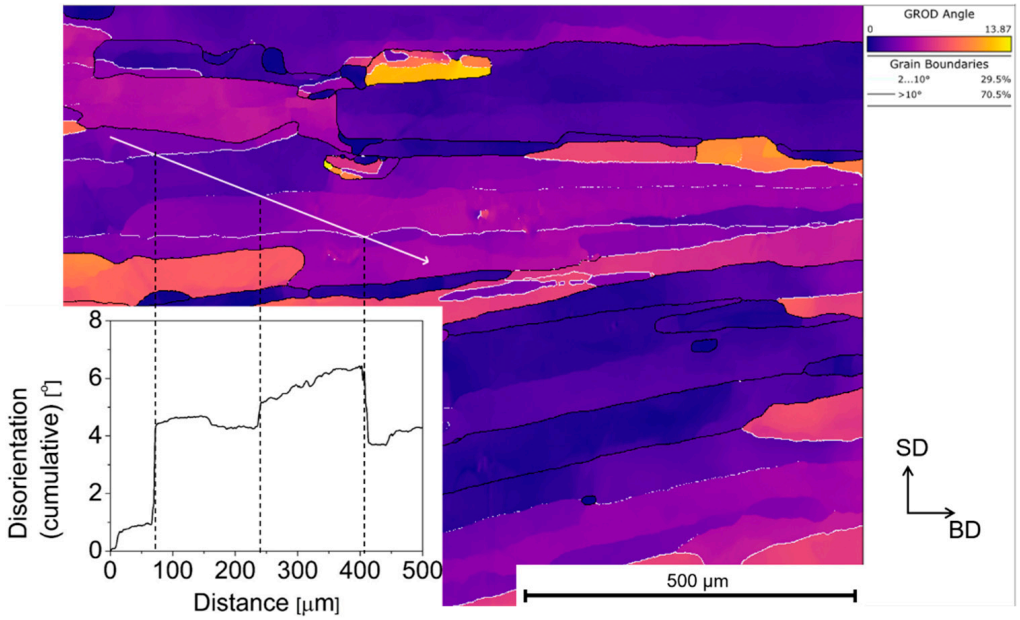

Figure 8. GROD-angle map visualizing local orientation deviations within grains, taken from the middle part of the L-PBF-fabricated sample. Inset shows cumulative disorientation in degrees along the white arrow across a coarse columnar grain. The BD and SD refer to the building and scanning directions. High- and low-angle grains are outlined with black and white boundaries. Grains were constructed assuming a 10° tolerance angle. The sample was printed with process parameters: P = 250 W and v_s = 1000 mm/s.

3.3. Bulk Hardness Testing

The Vickers hardness measurements were performed in several distinctive regions at the builds' bottom, middle, and top parts. Figure 9 shows the hardness spatial variation of as-built Fe_3AlTa alloys manufactured with L-PBF in comparison with those of the cast and SPS alloys. The results show that hardness varies from 371 to 346 HV across the build height. The lower hardness on the top layers may be attributed to a decrease in the strengthening Laves phase concentration, as shown in Figure 5. In the early stages of material built-up, ultra-fast cooling during L-PBF largely suppresses Ta segregation and the Laves phase formation and preserves the supersaturated Fe (Al, Ta) solid solution to lower temperatures. Upon further heating cycles, the Ta-enriched Laves phase precipitates both along the Fe-Al grains' boundaries and within the grains. Therefore, the higher hardness at the bottom of the builds may be ascribed to enhanced precipitation hardening due to the repetitive heating cycles experienced by the bottom region of the builds during the L-PBF process. A similar hardness variation with height caused by a difference in strengthening phase concentration was reported for direct laser-deposited alloy 718 builds [77,78]. In alloy 718, γ'' is not expected to form during initial rapid solidification but rather to develop during subsequent heating cycles; thus, the higher hardness at the bottom of the builds is observed.

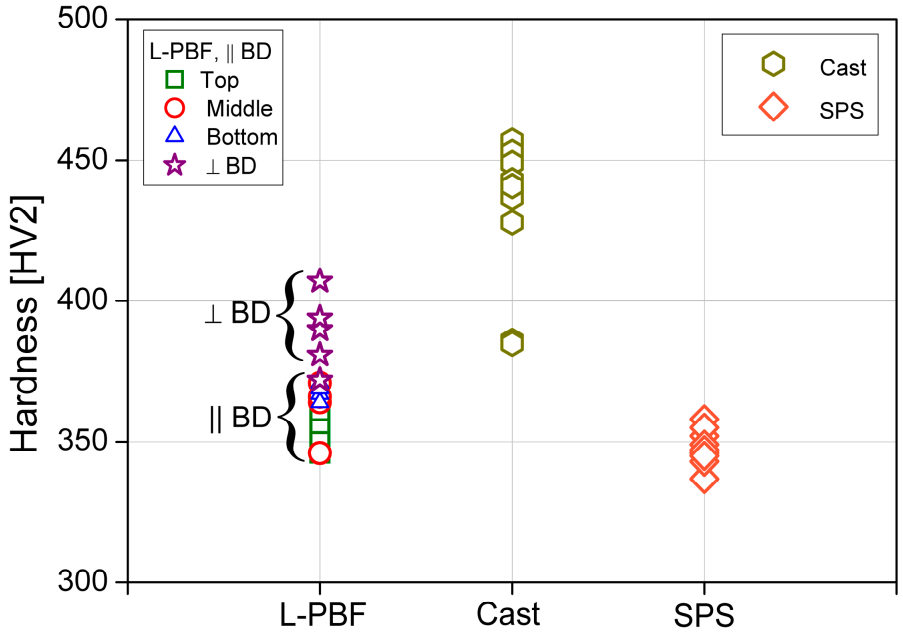

Figure 9. Vickers hardness (HV2) values of Fe_3Al-1.5Ta alloys manufactured by different methods of L-PBF, centrifugal investment casting, and spark plasma sintering (SPS). Spark plasma sintering was conducted at 1200 °C for a holding time of 5 s under a compaction force of 35 kN and L-PBF with process parameters P = 250 W and v_s = 1000 mm/s using a 67° layer-rotation strategy. Data for cast and SPS materials are shown for comparison. For more details on the microstructure of the as-cast and SPS materials, the readers are referred to references [14,47].

The hardness of the builds in the plane normal to the BD varies between 372 and 394 HV, indicating a negligible difference between hardness in planes parallel and perpendicular to the BD. The hardness values of the Fe_3Al-1.5Ta alloys do not show a substantial dependence on the manufacturing process. The L-PBF builds exhibit a hardness value comparable to the as-cast and spark plasma-sintered counterparts, though they possess quite different microstructures (for more details on the microstructure of the as-cast and SPS materials, the readers are referred to references [14,47]). Similar results for the binary Fe-28Al samples were reported, where the microhardness of SLM (353 ± 15 HV0.1) and

LMD (313 ± 13 HV0.1) builds was found quite comparable to values for as-cast Fe-27.6Al, with an average grain size of 290 µm [46,85].

The slightly lower hardness of the L-PBF Fe_3Al-1.5Ta builds than the cast material can be presumably attributed to AM-induced defects, such as porosity and the equiaxed grains of the as-cast material (grain boundaries effect on hardening). This conclusion is partly in line with the findings that show a significantly lower compressive yield stress for AM Fe-30Al-10Ti builds than an as-cast alloy from room temperature up to 600 °C [42].

The bulk literature results suggest that post-AM processing is required in addition to the employment of optimized AM process parameters to decrease the AM-induced defects and improve the mechanical performance of the AM parts [36,79,86]. A. Michalková et al. [42] investigated the laser AM of iron aluminides strengthened by various strategies of ordering (in Fe-30Al-10Ti), the precipitation of borides (in Fe-30Al-5Ti-0.7B), or the coherent $L2_1$ Heusler phase (in Fe-22Al-5Ti). They discovered that the mechanical properties of the builds are occasionally superior to the as-cast counterparts. The AM builds' yield stress and compressive creep strength matched the as-cast alloys above 600 °C. While at lower temperatures, higher yield stresses were observed in some cases, depending on the loading direction with respect to the building direction and post-heat treatment. No general improvement of ductility was observed in AM builds, specifically in the case of Fe–30Al–10Ti alloy, where the grain size in the builds was one order of magnitude less than in the as-cast alloy. The strength and ductility of some iron aluminide alloys could be markedly improved by AM through refinement of the microstructure and likely due to internal stresses.

The builds printed by L-PBF in the present study are composed of the non-uniform distribution of grains across the build height, from fine equiaxed grains at the very bottom layers to large ones at the middle and top layers. The elongated columnar microstructure resulting from the epitaxial growth is expected to reveal anisotropic mechanical properties in Fe_3Al-Ta builds, as reported for other iron aluminides [42,46]. A detailed investigation of the mechanical properties of the L-PBF builds compared to the as-cast material will be published elsewhere. Within the framework of the present study, we can surmise that the Fe_3AlTa builds should not be used directly after additive manufacturing without subjecting them to suitable post-manufacturing processing for grain refinement. Different grain refinement strategies, including alloy modification and post-processing thermal/thermomechanical treatments, can be considered for grain refining and improving the mechanical properties of the Fe_3AlTa builds to those of the cast alloys and beyond.

4. Conclusions

The current study investigates the laser powder bed fusion of Fe_3Al-1.5Ta alloy in terms of processability, microstructure, and hardness using SEM/EDX, EBSD, XRD, and Vickers hardness testing. Crack-free samples of anisotropic microstructures with densities higher than 99%, some approaching 99.5%, were fabricated from gas-atomized and pre-alloyed Fe-25Al-1.5Ta powders by L-PBF.

The melting and solidification dynamics lead to microstructures with large columnar grains, porosity, and periodic cracks during the printing process. Within the framework of this work, we demonstrated that the porosity and cracking issues could be resolved mainly by controlling the process parameters and preheating the build platform above the BDTT. The main findings of the current study are summarized as follows.

- The samples with the lowest values of porosity were obtained with a combination of high laser power (250–300 W), slow-to-medium scanning speeds (500–1000 mm/s), and 800 °C build plate preheating using a 67° rotation scanning strategy within the adapted parameters set (200–300 W/500–1500 mm/s);
- The morphology of the pores in the volume of the samples indicated a relatively sharp transition from spherical geometry for scanning speeds up to 1000 mm/s to crack-like pores for higher values;

- The L-PBF builds were characterized by coarse, columnar grains which grow epitaxially from the substrate, were several millimeters in width, and extended across several layers along the building direction. The grains exhibited a relatively strong microtexture close to <0 0 1> with respect to the building direction;
- XRD phase identification revealed a B2 FeAl-type order within a disordered A2 α-(Fe, Al) matrix decorated with Ta-rich (Fe, Al)$_2$Ta Laves phase precipitates (C14–P6$_3$/mmc);
- The builds contain a significant content of Laves phase particles finely dispersed within the grains in addition to the precipitates formed at the Fe-Al grain boundaries;
- Grain reference orientation deviation maps showed that individual grains were composed of a few sub-regions, with distinctive orientations correlated with the local lattice rotations arising from the high residual stress levels during L-PBF;
- The L-PBF builds showed a bulk hardness value comparable to the as-cast and spark plasma-sintered counterparts;
- The hardness exhibited minor variation across the build height, ranging from 346 to 371 HV.

Author Contributions: A.E.: conceptualization, investigation, writing—original draft, writing—review and editing, visualization; S.B.: investigation; J.B.: writing—review and editing; S.W.: supervision, writing—review and editing; M.B.: supervision, writing—review and editing. All authors have read and agreed to the published version of the manuscript.

Funding: The APC was funded by BTU Cottbus-Senftenberg and ETH Zurich.

Data Availability Statement: The data is available upon request from the corresponding authors.

Acknowledgments: A. Emdadi acknowledges the support from Panta Rhei gGmbH–Forschungszentrum für Leichtbauwerkstoffe (Cottbus-Germany) in the framework of a Postdoc Scholarship. The authors are thankful to Felix Jensch from HyF (BTU Cottbus-Senftenberg) for L-PBF operations and Michael Tovar from Helmholtz-Zentrum Berlin für Materialien und Energie GmbH for XRD.

Conflicts of Interest: The authors declare that they have no known competing financial interest or personal relationships that could have appeared to influence the work reported in this paper.

References

1. Palm, M.; Stein, F.; Dehm, G. Iron Aluminides. *Annu. Rev. Mater. Res.* **2019**, *49*, 297–326. [CrossRef]
2. Zamanzade, M.; Barnoush, A.; Motz, C. A Review on the Properties of Iron Aluminide Intermetallics. *Crystals* **2016**, *6*, 10. [CrossRef]
3. Peng, M.; Jasnau, S.; Palm, D.; Palm, M. Application of Iron Aluminides in the Combustion Chamber of Large Bore 2-Stroke Marine Engines. *Metals* **2019**, *9*, 847. [CrossRef]
4. McKamey, C.G. Iron Aluminides. In *Physical Metallurgy and Processing of Intermetallic Compounds*; Stoloff, N.S., Sikka, V.K., Eds.; Chapman & Hall: New York, NY, USA, 1996; pp. 351–391.
5. Morris, D.G.; Muñoz-Morris, M.A. Recent Developments Toward the Application of Iron Aluminides in Fossil Fuel Technologies. *Adv. Eng. Mater.* **2011**, *13*, 43–47. [CrossRef]
6. McKamey, C.G.; DeVan, J.H.; Tortorelli, P.F.; Sikka, V.K. A review of recent developments in Fe$_3$Al-based alloys. *J. Mater. Res.* **1991**, *6*, 1779–1805. [CrossRef]
7. McKamey, C.G.; Maziasz, P.J.; Jones, J.W. Effect of addition of molybdenum or niobium on creep-rupture properties of Fe$_3$Al. *J. Mater. Res.* **1992**, *7*, 2089–2106. [CrossRef]
8. Palm, M. Concepts derived from phase diagram studies for the strengthening of Fe-Al-based alloys. *Intermetallics* **2005**, *13*, 1286–1295. [CrossRef]
9. Schneider, A.; Sauthoff, G. Iron Aluminium Alloys with Strengthening Carbides and Intermetallic Phases for High-Temperature Applications. *Steel Res. Int.* **2004**, *75*, 55–61. [CrossRef]
10. Palm, M. Fe-Al materials for structural applications at high temperatures: Current research at MPIE. *IJMR* **2009**, *100*, 277–287. [CrossRef]
11. Yildirim, M.; Akdeniz, M.V.; Mekhrabov, A.O. Microstructural evolution and room-temperature mechanical properties of as-cast and heat-treated $Fe_{50}Al_{50}-$nNbn alloys (n = 1, 3, 5, 7, and 9 at.%). *Mater. Sci. Eng. A* **2016**, *664*, 17–25. [CrossRef]
12. Kratochvíl, P.; Švec, M.; Král, R.; Veselý, J.; Lukáč, P.; Vlasák, T. The Effect of Nb Addition on the Microstructure and the High-Temperature Strength of Fe$_3$Al Aluminide. *MMTA* **2018**, *49*, 1598–1603. [CrossRef]
13. Prokopčáková, P.; Švec, M.; Palm, M. Microstructural evolution and creep of Fe-Al-Ta alloys. *IJMR* **2016**, *107*, 396–405. [CrossRef]
14. Emdadi, A.; Sizova, I.; Bambach, M.; Hecht, U. Hot deformation behavior of a spark plasma sintered Fe-25Al-1.5Ta alloy with strengthening Laves phase. *Intermetallics* **2019**, *109*, 123–134. [CrossRef]
15. Prakash, U.; Sauthoff, G. Structure and properties of Fe-Al-Ti intermetallic alloys. *Intermetallics* **2001**, *9*, 107–112. [CrossRef]

16. Kratochvíl, P.; Kejzlar, P.; Král, R.; Vodičková, V. The effect of Zr addition on the structure and high temperature strength of Fe-30 at.% Al type alloys. *Intermetallics* **2012**, *20*, 39–46. [CrossRef]
17. Stein, F.; Leineweber, A. Laves phases: A review of their functional and structural applications and an improved fundamental understanding of stability and properties. *J. Mater. Sci.* **2021**, *56*, 5321–5427. [CrossRef]
18. Azmi, S.A.; Michalcová, A.; Senčekova, L.; Palm, M. Microstructure and mechanical properties of Fe-Al-Nb-B alloys. *MRS Adv.* **2017**, *2*, 1353–1359. [CrossRef]
19. Kratochvíl, P.; Vodičková, V.; Král, R.; Švec, M. The Effect of Laves Phase (Fe,Al)2Zr on the High-Temperature Strength of Carbon-Alloyed Fe_3Al Aluminide. *MMTA* **2016**, *47*, 1128–1131. [CrossRef]
20. Risanti, D.; Sauthoff, G. Microstructures and mechanical properties of Fe-Al-Ta alloys with strengthening Laves phase. *Intermetallics* **2011**, *19*, 1727–1736. [CrossRef]
21. Risanti, D.; Sauthoff, G. Iron–Aluminium-Base Alloys with Strengthening Laves Phase for Structural Applications at High Temperatures. *MSF* **2005**, *475–479*, 865–868. [CrossRef]
22. Hotař, A.; Palm, M. Oxidation resistance of Fe-25Al-2Ta (at.%) in air. *Intermetallics* **2010**, *18*, 1390–1395. [CrossRef]
23. Beaman, J.; Bourell, D.L.; Seepersad, C.; Kovar, D. Additive Manufacturing Review—Early Past to Current Practice. *J. Manuf. Sci. Eng.* **2020**, *142*, 110812. [CrossRef]
24. Ngo, T.D.; Kashani, A.; Imbalzano, G.; Nguyen, K.T.Q.; Hui, D. Additive Manufacturing (3D Printing): A Review of Materials, Methods, Applications and Challenges. *Compos. Part B Eng.* **2018**, *143*, 172–196. [CrossRef]
25. Tofail, S.A.M.; Koumoulos, E.P.; Bandyopadhyay, A.; Bose, S.; O'Donoghue, L.; Charitidis, C. Additive manufacturing: Scientific and technological challenges, market uptake and opportunities. *Mater. Today* **2018**, *21*, 22–37. [CrossRef]
26. Martin, J.H.; Yahata, B.D.; Hundley, J.M.; Mayer, J.A.; Schaedler, T.A.; Pollock, T.M. 3D printing of high-strength aluminium alloys. *Nature* **2017**, *549*, 365–369. [CrossRef]
27. Khorasani, M.; Ghasemi, A.; Rolfe, B.; Gibson, I. Additive manufacturing a powerful tool for the aerospace industry. *RPJ* **2022**, *28*, 87–100. [CrossRef]
28. Blakey-Milner, B.; Gradl, P.; Snedden, G.; Brooks, M.; Pitot, J.; Lopez, E.; Leary, M.; Berto, F.; Plessis, A.D. Metal additive manufacturing in aerospace: A review. *Mater. Des.* **2021**, *209*, 110008. [CrossRef]
29. Gu, D. Materials creation adds new dimensions to 3D printing. *Sci. Bull.* **2016**, *61*, 1718–1722. [CrossRef]
30. Sun, C.; Wang, Y.; McMurtrey, M.D.; Jerred, N.D.; Liou, F.; Li, J. Additive manufacturing for energy: A review. *Appl. Energy* **2021**, *282*, 116041. [CrossRef]
31. Verhoef, L.A.; Budde, B.W.; Chockalingam, C.; Nodar, B.G.; van Wijk, A.J.M. The effect of additive manufacturing on global energy demand: An assessment using a bottom-up approach. *Energy Policy* **2018**, *112*, 349–360. [CrossRef]
32. Frazier, W.E. Metal Additive Manufacturing: A Review. *J. Mater. Eng. Perform.* **2014**, *23*, 1917–1928. [CrossRef]
33. Griffiths, S.; Croteau, J.R.; Rossell, M.D.; Erni, R.; de Luca, A.; Vo, N.Q.; Dunand, D.C.; Leinenbach, C. Coarsening- and creep resistance of precipitation-strengthened Al–Mg–Zr alloys processed by selective laser melting. *Acta Mater.* **2020**, *188*, 192–202. [CrossRef]
34. Carter, L.N.; Martin, C.; Withers, P.J.; Attallah, M.M. The influence of the laser scan strategy on grain structure and cracking behaviour in SLM powder-bed fabricated nickel superalloy. *J. Alloys Compd.* **2014**, *615*, 338–347. [CrossRef]
35. Lewandowski, J.J.; Seifi, M. Metal Additive Manufacturing: A Review of Mechanical Properties. *Annu. Rev. Mater. Sci.* **2016**, *46*, 151–186. [CrossRef]
36. Hosseini, E.; Popovich, V. A review of mechanical properties of additively manufactured Inconel 718. *Addit. Manuf.* **2019**, *30*, 100877. [CrossRef]
37. Kakehi, K.; Banoth, S.; Kuo, Y.-L.; Hayashi, S. Effect of yttrium addition on creep properties of a Ni-base superalloy built up by selective laser melting. *Scr. Mater.* **2020**, *183*, 71–74. [CrossRef]
38. Linares, J.-M.; Chaves-Jacob, J.; Lopez, Q.; Sprauel, J.-M. Fatigue life optimization for 17-4Ph steel produced by selective laser melting. *RPJ* **2022**, *28*, 1182–1192. [CrossRef]
39. Giganto, S.; Martínez-Pellitero, S.; Cuesta, E.; Zapico, P.; Barreiro, J. Proposal of design rules for improving the accuracy of selective laser melting (SLM) manufacturing using benchmarks parts. *Rapid Prototyp. J.* **2022**, *28*, 1129–1143. [CrossRef]
40. Shen, C.; Pan, Z.; Ma, Y.; Cuiuri, D.; Li, H. Fabrication of iron-rich Fe-Al intermetallics using the wire-arc additive manufacturing process. *Addit. Manuf.* **2015**, *7*, 20–26. [CrossRef]
41. Shen, C.; Reid, M.; Liss, K.-D.; Pan, Z.; Ma, Y.; Cuiuri, D.; van Duin, S.; Li, H. Neutron diffraction residual stress determinations in Fe_3Al based iron aluminide components fabricated using wire-arc additive manufacturing (WAAM). *Addit. Manuf.* **2019**, *29*, 100774. [CrossRef]
42. Michalcová, A.; Senčekova, L.; Rolink, G.; Weisheit, A.; Pešička, J.; Stobik, M.; Palm, M. Laser additive manufacturing of iron aluminides strengthened by ordering, borides or coherent Heusler phase. *Mater. Des.* **2017**, *116*, 481–494. [CrossRef]
43. Pęska, M.; Karczewski, K.; Rzeszotarska, M.; Polański, M. Direct Synthesis of Fe-Al Alloys from Elemental Powders Using Laser Engineered Net Shaping. *Materials* **2020**, *13*, 531. [CrossRef] [PubMed]
44. Durejko, T.; Ziętala, M.; Łazińska, M.; Lipiński, S.; Polkowski, W.; Czujko, T.; Varin, R.A. Structure and properties of the Fe_3Al-type intermetallic alloy fabricated by laser engineered net shaping (LENS). *Mater. Sci. Eng. A* **2016**, *650*, 374–381. [CrossRef]
45. Kwiatkowska, M.; Zasada, D.; Bystrzycki, J.; Polański, M. Synthesis of Fe-Al-Ti Based Intermetallics with the Use of Laser Engineered Net Shaping (LENS). *Materials* **2015**, *8*, 2311–2331. [CrossRef]
46. Rolink, G.; Vogt, S.; Senčekova, L.; Weisheit, A.; Poprawe, R.; Palm, M. Laser metal deposition and selective laser melting of Fe–28 at.% Al. *J. Mater. Res.* **2014**, *29*, 2036–2043. [CrossRef]

47. Emdadi, A. *High-Temperature Deformation Behavior of Intermetallic Titanium and Iron Aluminides Produced by Spark Plasma Sintering*, 1st ed.; Shaker: Düren, Germnay, 2021.
48. Kenel, C.; Lis, A.; Dawson, K.; Stiefel, M.; Pecnik, C.; Barras, J.; Colella, A.; Hauser, C.; Tatlock, G.J.; Leinenbach, C.; et al. Mechanical performance and oxidation resistance of an ODS γ-TiAl alloy processed by spark plasma sintering and laser additive manufacturing. *Intermetallics* **2017**, *91*, 169–180. [CrossRef]
49. Risanti, D.; Sauthoff, G. Strengthening of iron aluminide alloys by atomic ordering and Laves phase precipitation for high-temperature applications. *Intermetallics* **2005**, *13*, 1313–1321. [CrossRef]
50. Sizova, I.; Sviridov, A.; Bambach, M.; Eisentraut, M.; Hemes, S.; Hecht, U.; Marquardt, A.; Leyens, C. A study on hot-working as alternative post-processing method for titanium aluminides built by laser powder bed fusion and electron beam melting. *J. Mater. Process. Technol.* **2021**, *291*, 117024. [CrossRef]
51. Witusiewicz, V.T.; Bondar, A.A.; Hecht, U.; Zollinger, J.; Petyukh, V.M.; Fomichov, O.S.; Voblikov, V.M.; Rex, S. Experimental study and thermodynamic re-assessment of the binary Al–Ta system. *Intermetallics* **2010**, *18*, 92–106. [CrossRef]
52. Witusiewicz, V.; Bondar, A.; Hecht, U.; Voblikov, V.; Fomichov, O.; Petyukh, V.; Rex, S. Experimental study and thermodynamic re-assessment of the binary Fe-Ta system. *Intermetallics* **2011**, *19*, 1059–1075. [CrossRef]
53. Wright, S.I.; Nowell, M.M.; Field, D.P. A Review of Strain Analysis Using Electron Backscatter Diffraction. *Microsc. Microanal.* **2011**, *17*, 316–329. [CrossRef] [PubMed]
54. Gu, D.; Hagedorn, Y.-C.; Meiners, W.; Meng, G.; Batista, R.J.S.; Wissenbach, K.; Poprawe, R. Densification behavior, microstructure evolution, and wear performance of selective laser melting processed commercially pure titanium. *Acta Mater.* **2012**, *60*, 3849–3860. [CrossRef]
55. Coeck, S.; Bisht, M.; Plas, J.; Verbist, F. Prediction of lack of fusion porosity in selective laser melting based on melt pool monitoring data. *Addit. Manuf.* **2019**, *25*, 347–356. [CrossRef]
56. Singla, A.K.; Banerjee, M.; Sharma, A.; Singh, J.; Bansal, A.; Gupta, M.K.; Khanna, N.; Shahi, A.S.; Goyal, D.K. Selective laser melting of Ti6Al4V alloy: Process parameters, defects and post-treatments. *J. Manuf. Process.* **2021**, *64*, 161–187. [CrossRef]
57. Gong, H.; Rafi, K.; Gu, H.; Ram, G.D.J.; Starr, T.; Stucker, B. Influence of defects on mechanical properties of Ti–6Al–4V components produced by selective laser melting and electron beam melting. *Mater. Des.* **2015**, *86*, 545–554. [CrossRef]
58. Sabzi, H.E.; Rivera-Díaz-Del-Castillo, P.E.J. Defect Prevention in Selective Laser Melting Components: Compositional and Process Effects. *Materials* **2019**, *12*, 3791. [CrossRef]
59. Fatemi, A.; Molaei, R.; Simsiriwong, J.; Sanaei, N.; Pegues, J.; Torries, B.; Phan, N.; Shamsaei, N. Fatigue behaviour of additive manufactured materials: An overview of some recent experimental studies on Ti-6Al-4V considering various processing and loading direction effects. *Fatigue Fract. Eng. Mater. Struct.* **2019**, *42*, 991–1009. [CrossRef]
60. Nudelis, N.; Mayr, P. A Novel Classification Method for Pores in Laser Powder Bed Fusion. *Metals* **2021**, *11*, 1912. [CrossRef]
61. Kubaschewski, O. *Iron—Binary Phase Diagrams*; Springer Science & Business Media: New York, NY, USA, 2013.
62. Köster, W.; Gödecke, T. Physikalische Messungen an Eisen-Aluminium-Legierungen mit 10 bis 50 At.% Al. *IJMR* **1980**, *71*, 765–769. [CrossRef]
63. Inden, G.; Pepperhoff, W. Experimental Study of the Order—Disorder Transition in bcc Fe-Al Alloys/Experimentelle Untersuchung des Übergangs geordnet-ungeordnet in krz Fe-Al-Legierungen. *Int. J. Mater. Res.* **1990**, *81*, 770–773. [CrossRef]
64. Palm, M.; Lacaze, J. Assessment of the Al-Fe-Ti system. *Intermetallics* **2006**, *14*, 1291–1303. [CrossRef]
65. Witusiewicz, V.T.; Bondar, A.A.; Hecht, U.; Voblikov, V.M.; Tsyganenko, N.I.; Fomichov, O.S.; Karpets, M.V.; Petyukh, V.M.; Velikanova, T.Y. Experimental study and thermodynamic modelling of the ternary Al-Fe-Ta system. *J. Mater. Sci.* **2013**, *48*, 377–412. [CrossRef]
66. Marker, M.C.J.; Duarte, L.I.; Leinenbach, C.; Richter, K.W. Characterization of the Fe-rich corner of Al-Fe-Si-Ti. *Intermetallics* **2013**, *39*, 38–49. [CrossRef] [PubMed]
67. Łazińska, M.; Durejko, T.; Zasada, D.; Bojar, Z. Microstructure and mechanical properties of a Fe-28%Al-5%Cr-1%Nb-2%B alloy fabricated by Laser Engineered Net Shaping. *Mater. Lett.* **2017**, *196*, 87–90. [CrossRef]
68. Golovin, I.S.; Emdadi, A.; Balagurov, A.M.; Bobrikov, I.A.; Cifre, J.; Zadorozhnyy, M.Y.; Rivière, A. Anelasticity of iron-aluminide Fe_3Al type single and polycrystals. *J. Alloys Compd.* **2018**, *746*, 660–669. [CrossRef]
69. Golovin, I.S.; Balagurov, A.M.; Bobrikov, I.A.; Cifre, J. Structure induced anelasticity in Fe_3Me (Me = Al, Ga, Ge) alloys. *J. Alloys Compd.* **2016**, *688*, 310–319. [CrossRef]
70. Pütz, R.D.; Zander, D. High temperature oxidation mechanisms of grain refined Fe-25Al-1.5Ta(+TaC/+(Ta,Nb)C) iron aluminides at 700 °C in air. *Corros. Sci.* **2022**, *198*, 110149. [CrossRef]
71. Balagurov, A.M.; Bobrikov, I.A.; Sumnikov, S.V.; Golovin, I.S. Antiphase domains or dispersed clusters? Neutron diffraction study of coherent atomic ordering in Fe_3Al-type alloys. *Acta Mater.* **2018**, *153*, 45–52. [CrossRef]
72. Collins, P.C.; Brice, D.A.; Samimi, P.; Ghamarian, I.; Fraser, H.L. Microstructural Control of Additively Manufactured Metallic Materials. *Annu. Rev. Mater. Res.* **2016**, *46*, 63–91. [CrossRef]
73. Shen, C.; Pan, Z.; Cuiuri, D.; Dong, B.; Li, H. In-depth study of the mechanical properties for Fe_3Al based iron aluminide fabricated using the wire-arc additive manufacturing process. *Mater. Sci. Eng. A* **2016**, *669*, 118–126. [CrossRef]
74. Song, B.; Dong, S.; Coddet, P.; Liao, H.; Coddet, C. Fabrication and microstructure characterization of selective laser-melted FeAl intermetallic parts. *Surf. Coat. Technol.* **2012**, *206*, 4704–4709. [CrossRef]
75. Liu, P.; Wang, Z.; Xiao, Y.; Horstemeyer, M.F.; Cui, X.; Chen, L. Insight into the mechanisms of columnar to equiaxed grain transition during metallic additive manufacturing. *Addit. Manuf.* **2018**, *26*, 22–29. [CrossRef]

76. Berminghama, M.J.; StJohnab, D.H.; Krynena, J.; Tedman-Jonesa, S.; Darguschab, M.S. Promoting the columnar to equiaxed transition and grain refinement of titanium alloys during additive manufacturing. *Acta Mater.* **2019**, *168*, 261–274. [CrossRef]
77. Tian, Y.; McAllister, D.; Colijn, H.; Mills, M.; Farson, D.; Nordin, M.; Babu, S. Rationalization of Microstructure Heterogeneity in INCONEL 718 Builds Made by the Direct Laser Additive Manufacturing Process. *Met. Mater. Trans. A* **2014**, *45*, 4470–4483. [CrossRef]
78. Stevens, E.L.; Toman, J.; To, A.C.; Chmielus, M. Variation of hardness, microstructure, and Laves phase distribution in direct laser deposited alloy 718 cuboids. *Mater. Des.* **2017**, *119*, 188–198. [CrossRef]
79. Schwalbach, E.J.; Donegan, S.P.; Chapman, M.G.; Chaput, K.J.; Groeber, M.A. A discrete source model of powder bed fusion additive manufacturing thermal history. *Addit. Manuf.* **2018**, *25*, 485–498. [CrossRef]
80. Karczewski, K.; Durejko, T.; Czujko, T. The Microstructure Evolution of a Fe_3Al Alloy during the LENS Process. *Materials* **2018**, *11*, 390. [CrossRef]
81. Vilaro, T.; Kottman-Rexerodt, V.; Thomas, M.; Colin, C.; Bertrand, P.; Thivillon, L.; Abed, S.; Ji, V.; Aubry, P.; Peyre, P.; et al. Direct Fabrication of a Ti-47Al-2Cr-2Nb Alloy by Selective Laser Melting and Direct Metal Deposition Processes. *Adv. Mater. Res.* **2010**, *89–91*, 586–591. [CrossRef]
82. Bartlett, J.L.; Li, X. An overview of residual stresses in metal powder bed fusion. *Addit. Manuf.* **2019**, *27*, 131–149. [CrossRef]
83. Terner, M.; Lee, J.; Marchese, G.; Biamino, S.; Hong, H.-U. Electron Backscattered Diffraction to Estimate Residual Stress Levels of a Superalloy Produced by Laser Powder Bed Fusion and Subsequent Heat Treatments. *Materials* **2020**, *13*, 4643. [CrossRef]
84. Nolze, G.; Winkelmann, A. About the reliability of EBSD measurements: Data enhancement. *IOP Conf. Ser. Mater. Sci. Eng.* **2020**, *891*, 012018. [CrossRef]
85. Sundar, R.S.; Kutty, T.R.G.; Sastry, D.H. Hot hardness and creep of Fe_3Al-based alloys. *Intermetallics* **2000**, *8*, 427–437. [CrossRef]
86. Hackel, J.R.L.; Rankin, A.; Rubenchik, W.E.; King, M. Matthews. Laser peening: A tool for additive manufacturing post-processing. *Addit. Manuf.* **2018**, *24*, 67–75. [CrossRef]